Wavy nature of collagen fibrils deduced from the dispersion of their second-order nonlinear optical anisotropy parameters ρ.

Denis Rouède, Emmanuel Schaub, Jean-Jacques Bellanger, Frederic Ezan, François Tiaho

Research Article | Vol. 28, No. 4 / 17 February 2020 / Optics Express 4845
Optics EXPRESS

Wavy nature of collagen fibrils deduced from the dispersion of their second-order nonlinear optical anisotropy parameters ρ

DENIS ROUÈDE,[1,*] EMMANUEL SCHAUB,[1] JEAN-JACQUES BELLANGER,[2] FRÉDÉRIC EZAN,[3] AND FRANÇOIS TIAHO[3]

[1]CNRS, Institut de Physique de Rennes, Département Matière molle, UMR UR1-CNRS 6251, Université de Rennes1, F-35042 Rennes, France
[2]INSERM, Laboratoire Traitement du Signal et de l'Image, UMR UR1-INSERM U642, Université de Rennes1, F-35042 Rennes, France
[3]INSERM, UMR1085, IRSET Institut de Recherche sur la Santé l'Environnement et le Travail, SFR Biosit, Université de Rennes1, F-35043 Rennes, France
*denis.rouede@univ-rennes1.fr

Abstract: From P-SHG experiments, second-order nonlinear optical anisotropy parameters $\rho = \chi_{ZZZ}/\chi_{ZXX}$ of collagen tissues are calculated assuming the same model of supercoiled collagen fibril characterized by a variable angle θ. Dispersion of experimental ρ values is converted into distribution of θ values based on the wavy nature of collagen fibrils deduced from EM studies. For tendon, the results show that the dispersion of experimental ρ values is mainly due to Poisson photonic shot noise assuming a slight fibrillar undulation with $\theta = 2.2^{\circ} \pm 1.8^{\circ}$. However for skin and vessels, the dispersion of experimental ρ values is mainly due to a stronger fibrillar undulation with $\theta = 16.2^{\circ} \pm 1.3^{\circ}$. The results highlight that this undulation is reduced during the development of liver fibrosis therefore, contributing to the rigidity of the tissue.

1. Introduction

Second harmonic generation (SHG) microscopy is a label-free technique that relies on a nonlinear optical interaction with hyperpolarizable non-centrosymmetric endogenous fibrillar proteins like collagen and myosin causing scattered coherent radiation at twice the fundamental frequency [1–4]. Polarization dependence of SHG (P-SHG) microscopy is gaining increase popularity for investigating fibrillar collagen-rich tissues with the desire to extract structural information in both physiological and disease states. Organization of collagen fibrils is usually described by the SHG anisotropy parameter ρ, which is related to the SHG intensity ratios measured for the directions of the excitation fields parallel and perpendicular to the axis of the collagen fibrils [5–13].

We previously proposed a simple reliable and fast linear least square (LLS) fitting method to process P-SHG images at pixel-resolution [14]. More recently, we extended this method to retrieve the pixel-resolved sub-microscopic organization of fibrillar collagen molecules taking into account the background Poisson photonic shot noise of the detectors and the poly helical architecture (helix, triple helix, supercoil) of collagen fibrils. Correlation between experimental and theoretical statistical distributions of ρ values through a Monte Carlo simulation was used to estimate the fibrillar disorder in the SHG image. In this previous model, we assumed that it was due to a random tilt of each fibril contained in the pixel [15]. However, with this model we could not accurately report dispersion of experimental ρ values in liver vessels assuming supercoiled tropocollagen molecules twisted at a constant polar angle θ.

The aim of the present work is a significant upgrade of our model to rigorously explain the dispersion of experimental ρ values by considering a pixel by pixel change of polar angle θ. We find that the dispersion of ρ values is the result of a slight fibrillar undulation with $\theta = 2.2^{\circ} \pm 1.8^{\circ}$

#380089 https://doi.org/10.1364/OE.380089
Journal © 2020 Received 11 Oct 2019; revised 22 Dec 2019; accepted 2 Jan 2020; published 7 Feb 2020

Optics EXPRESS

in tendon. However for skin and vessels, the fibrillar undulation is stronger with $\theta = 16.2° \pm 1.3°$. Moreover, in liver vessels, development of fibrosis is characterized by a significant reduction of θ supporting the increase rigidity of the vessels.

2. Materials and methods

2.1. Preparation of biological samples

Samples from physiological and pathological tissues were prepared as previously reported and summarized as follows [15]. Physiological samples were prepared from rat extensor digitorum longus (EDL) tendon, rat skin and mouse liver vessels. Adult Wistar rats (200-300 g) were euthanized by CO_2 inhalation. Tissues were dissected, fixed over night with 4% paraformaldehyde in phosphate buffer saline at 4°C, and rinsed at least three times with PBS. For SHG imaging, dissected pieces (100-200 μm thickness) of tissues were mounted in 50% glycerol-PBS solution and stabilized between two coverslips sealed with nail polish. For pathological samples, wild-type C57BL/6J mice received intraperitoneal injection of either 0,5 µg CCl_4 (Sigma, St Louis, MO) dissolved in oil in order to induce liver fibrosis or the olive oil solvent for control mice. Injections were performed 3 times (D1, D3 and D7) the first week followed by single injection every week lasting 8 weeks (W1-W8). Mice were euthanized at D1 or at W10, livers were harvested and fixed in 4% paraformaldehyde. For SHG-imaging, 10 μm thick sections of liver slices mounted between microscope glass slides and coverslips were obtained from the Biosit-H2P2 core (histopathologie.univ-rennes1.fr/) according to established standard procedure. All rats and mice were cared for in accordance to the "Guide for the Care and Use of Laboratory Animals" (Directive 2010/63/UE).

2.2. Image acquisition and analysis

Images were acquired on a custom made SHG microscope part of the BIOSIT facility https://biosit.univ-rennes1.fr. It is based on an inverted microscope (IX71, Olympus, Japan) and the laser source is a tunable IR 80 MHz femtosecond Ti:Sa laser (MAITAI, Spectra Physics). High NA water immersion objective (Olympus UPLSAPO 60XW NA = 1.20, WD = 0.28 mm) was used for applying 10-20 mW of 740 nm excitation at the sample. PSF was obtained from 0.17 μm diameter fluorescent micro beads (Molecular Probes PS-Speck Microscope Point Source Kit (P7220)) and estimated to be 0.4×1.2 μm. SHG signal was collected in forward direction using high NA objective (Olympus, LUMFl 60XW, NA = 1.1). SHG signal is detected using high sensitivity single photon GasAsP photomultipliers (H7421-40, Hamamatsu). Photons are counted by a general-purpose acquisition USB module (NI-USB 6363, National Instruments). It is important to note that in addition to tissue clearing obtained with 50% glycerol treatment, all polarization dependent SHG images were acquired at a depth < 20 µm from the tissue surface to minimize depolarization [16] and birefringence effects [17,18]. All experimental P-SHG stacks were obtained for input polarization angles uniformly distributed between 0° and 180° with 20° increments. This incremental step is a good sampling compromise for accurate acquisition of P-SHG parameters and quality of the recording, avoiding motion artifact. Image analysis and simulations were performed using MALAB (MathWorks, Natick, MA, USA).

3. Theory

Nonlinear molecular response of collagen tissues can be described by the hyperpolarizability response of tropocollagen triple helix molecules [19] that assemble in a quarter-staggered array to form microfibrils [20]. Moreover, it is known that collagen fibrils can be straight as in tendon or supercoiled as in skin and vessels [21–27]. In this latter case, the triple helices are wrapped with an angle θ around the main axis Z of the fibril in the fibrillar coordinate system (X, Y, Z), (Fig. 1(a)).

Optics EXPRESS

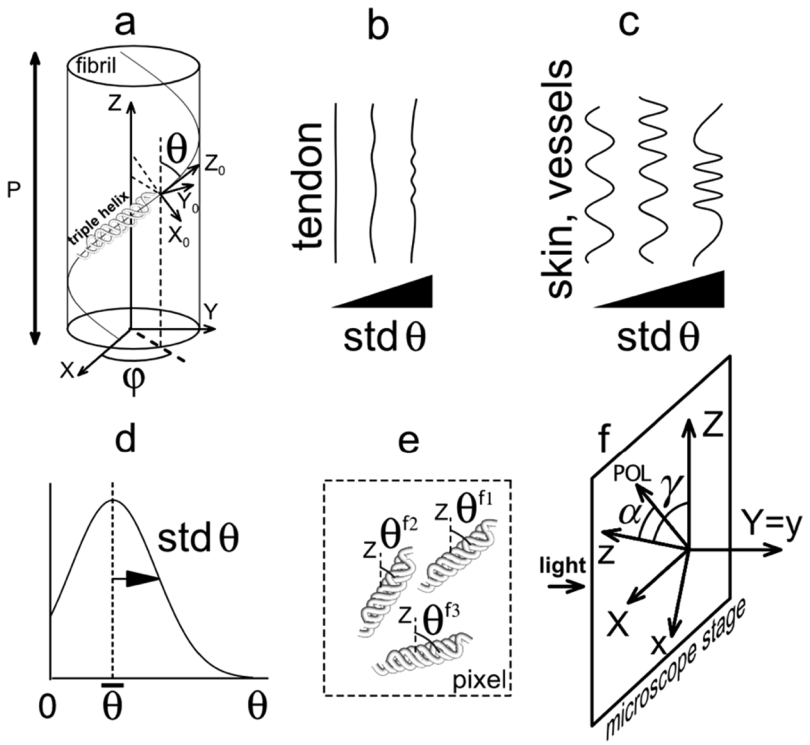

Fig. 1. Schematic diagram of a collagen fibril. (a) Representation of the triple helix of a supercoil collagen fibril. (X_0, Y_0, Z_0) and (X, Y, Z) are the reference frames of respectively the triple helix and of the supercoil collagen fibril and Z_0 and Z are their respective main directions. θ and φ refer to the polar and azimuthal angles and P is the pitch corresponding to a full turn of the coiling. Schematic diagram illustrating the waving of collagen fibrils in tendon (b) and in skin or vessels (c) with increasing pixel by pixel dispersion $std\,\theta$ of supercoil angles θ from left to right. (d) Truncated normal (Gaussian) distribution of supercoil angles θ with parameters $\bar{\theta}$ and $std\,\theta$ of the normal distribution. (e) Schematic view of intra pixel disorder. In this illustration, the pixel contains three fibrils different polar angles ($\theta^{f1}, \theta^{f2}, \theta^{f3}$). Note that each fibril is represented by one of its triple helix molecule. (f) Schematic view of the microscope stage. Z is the main fibrillar direction supposed to be in the plane of the microscope stage, and forming an angle γ with the fixed direction z of the laboratory coordinate system (x, y, z). Polarization of the incident IR beam (POL) makes an angle α with z. Light propagates along Y = y.

Optics EXPRESS

In the following, we choose to represent straight and supercoiled fibrils by the same model of fibril with a variable supercoil angle θ according to the collagen tissue : $\theta \simeq 0°$ for tendon and $\theta \simeq 17°$ for skin and vessels. This is consistent with the fact that collagen fibrils are more or less coiled (for review see [21]). Moreover, waving or undulating collagen fibrils were also observed in liver [28] and in tendon from EM studies [24,29–31]. From EM results, we hypothesize that the wavy nature of collagen fibrils could be modeled by a pixel by pixel dispersion of the supercoil angle θ. A schematic diagram illustrating the waving of collagen fibrils is shown for tendon (Fig. 1(b)) and for skin or vessels (Fig. 1(c)). The increasing dispersion of supercoil angles θ from left to right corresponds to an increasing fibrillar undulation. This fibrillar waving is simply modeled here by a truncated normal (Gaussian) distribution of supercoil angles θ centered around mean value $\overline{\theta}$ with dispersion *std* θ (Fig. 1(d)). These parameters correspond to the parameters of the normal distribution without truncation which should not be confused with the mean and standard deviation of the truncated normal distribution.

In the hypothesis of a possible intra pixel fibrillar angular disorder, we next assume that each pixel may contain N_f fibrils having triple helices with different polar angles θ^f (Fig. 1(e)), always measured with the same common direction Z supposed to be in the plane of the microscope stage (Fig. 1(f)). These angles are randomly chosen in the same truncated normal distribution of parameters $\overline{\theta}$ and $std\theta$ for simplicity. In this context, we calculated the second-order nonlinear optical susceptibility $\chi^{(2)}$ at pixel level by summing the contribution of all triple helices in the focusing volume. We found (see Appendix) that for an incident IR beam propagating in the Y direction (Fig. 1(f)), only two independent second-order nonlinear optical susceptibility coefficients χ_{ZZZ} and $\chi_{ZXX} = \chi_{XXZ} = \chi_{XZX}$ mainly contribute to the SHG signal when expressed in coordinate system (X, Y, Z). The resulting SHG anisotropy parameter $\rho_{th} = \chi_{ZZZ}/\chi_{ZXX}$ is given by

$$\rho_{th} = \frac{\rho_0 \left\langle \cos\theta^f \right\rangle + (3-\rho_0)\left\langle \cos\theta^f \sin^2\theta^f \right\rangle}{\left\langle \cos\theta^f \right\rangle - (3-\rho_0)\left\langle \left\langle \cos^2\varphi \right\rangle_f \cos\theta^f \sin^2\theta^f \right\rangle}, \tag{1}$$

where $\left\langle h(\theta^f) \right\rangle$ and $\left\langle \cos^2\varphi \right\rangle_f$ are also defined in the Appendix. These coefficients correspond respectively to the summation made on the N_f fibrils f contained in the pixel and to a mean value made on the azimuthal angle φ on the part of the fibril f that is contained in the transverse PSF. ρ_0 is defined as the anisotropy parameter of the triple helix [9,12,32]. Under these conditions, the SHG intensity is given by the usual formula [5–14,32–40]

$$I^{2\omega}(\alpha) \propto [\sin 2(\gamma-\alpha)]^2 + [\sin^2(\gamma-\alpha) + \rho_{th}\cos^2(\gamma-\alpha)]^2, \tag{2}$$

where α and γ are the angles of respectively the directions of the input polarization (POL) and of the main fibril axis Z with a common direction z of the laboratory coordinate system (x, y, z), (Fig. 1(f)).

On the other hand, we have also previously shown that it is important to take into account the contribution of Poisson photonic shot noise of the detection system to minimize correlation errors between experimental and theoretical results [15]. For this reason, a Poisson noise anisotropy parameter, named ρ_{poiss} in the following, is deduced from ρ_{th} for correlation with experimental anisotropy parameters $\rho_{\exp}$ calculated by LLS fitting method of the P-SHG stack [14]. The procedure to calculate ρ_{poiss} starts with the calculation of $I^{2\omega}(\alpha)$ at given ρ_{th} considering the proportionality factor as unity in Eq. (2). A Poisson noise P-SHG intensity curve $I^{poiss}(\alpha)$ is then simulated by generating for each α (0°, 20°,40°. . . 180°, see section Materials and methods) a Poisson distributed random variable with a Poisson parameter (mean of the Poisson distribution) equals to $N_{ph} \times I^{2\omega}(\alpha)/\overline{I^{2\omega}}$. N_{ph} and $\overline{I^{2\omega}}$ respectively correspond to the averages on α of the number of photons per pixel and of $I^{2\omega}(\alpha)$. Finally, ρ_{poiss} is deduced from $I^{poiss}(\alpha)$ using LLS fitting method [14].

Optics EXPRESS

4. Model simulation results

Figure 2(a) illustrates the impact of θ on ρ_{th} in the case of no intra pixel fibrillar angular disorder, when all fibrils within the pixel have the same polar angle θ.

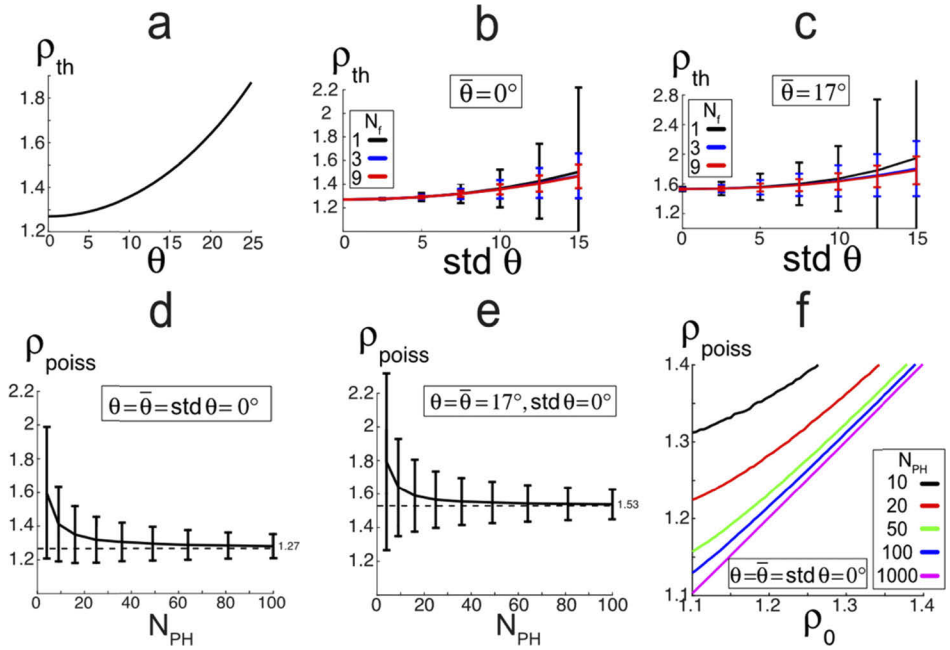

Fig. 2. Theoretical simulation of ρ_{th} and ρ_{poiss}. (a) Evolution of ρ_{th} as a function of θ for the particular case of no fibrillar disorder *std* θ and for $<\cos^2\varphi> = \frac{1}{2}$. (b, c) Impact of increasing *std* θ on ρ_{th} for straight ($\bar{\theta} = 0°$) (b) and supercoiled ($\bar{\theta} = 17°$) (c) fibrils for the number of fibrils per pixel N_f indicated in the inset. (d, e) Evolution of ρ_{poiss} for straight $\theta = \bar{\theta} = 0°$(d) and supercoiled fibrils $\theta = \bar{\theta} = 17°$ (e) as a function of the P-SHG stack mean photon number per pixel N_{ph} assuming no angular dispersion *std* $\theta = 0°$. For straight fibrils, ρ_{poiss} is calculated from $\rho_{th} = \rho_0 = 1.27$ corresponding to the experimental values obtained in tendon at high photon level N_{ph}=100 (dotted line, see also section Experimental results). For supercoiled fibrils, ρ_{poiss} is calculated from $\rho_{th} = \rho_0 = 1.53$ ($\theta = 17°$) corresponding to the experimental values obtained in skin at high photon level N_{ph}=100 (dotted line, see also section Experimental results). (f) Evolution of ρ_{poiss} as a function of ρ_0 for perfectly aligned straight fibrils θ = *std*$\theta = 0°$ and for different N_{ph}. For b-e, mean value (solid lines) and dispersion (vertical bars) are obtained from 10 000 trials.

The result shows that ρ_{th} increases with θ similarly to the case of increase fibrillar tilting [11]. We next model the impact of *std*θ on ρ_{th} for tendon ($\bar{\theta} = 0°$, Fig. 2(b)) and skin ($\bar{\theta} = 17°$, Fig. 2(c)). The impact of intra pixel fibrillar angular disorder is also taken into account considering a variable number N_f (1, 3, 9) of fibrils in the pixel with different polar angles θ^f. The main finding is that increasing *std* θ, reflecting a growing angular waving of the fibrils, results in an increase of mean value of ρ_{th} and its dispersion *std* ρ_{th}. However, increasing N_f progressively reduced *std* ρ_{th} towards zero. Taking into account Poisson photonic shot noise, we next model the evolution of ρ_{poiss} as a function of the P-SHG stack mean photon number per pixel N_{ph} for tendon ($\bar{\theta} = 0°$, Fig. 2(d)) and skin ($\bar{\theta} = 17°$, Fig. 2(e)) assuming no angular dispersion *std* $\theta = 0$. For both cases, we observe that, whereas *std* ρ_{poiss}decreases approximately as the inverse of the square root of N_{ph} (as classically expected), the corresponding estimation of mean ρ_{poiss}decreases asymptotically toward ρ_0. One should notice that a bias due to Poisson noise is clearly visible for $N_{ph} < 40$.

Optics EXPRESS

This bias is further highlighted in Fig. 2(f) for well aligned straight fibrils $\bar{\theta} = 0$, $std\theta = 0$. In accordance with Figs. 2(d) and 2(e), this bias is significantly reduced for $N_{ph} > 50$. This shows that N_{ph} must be greater than 100 to reduce the bias below 1% in order to accurately determine ρ_0 from experimental results.

5. Experimental results

Our objective in this section is to determine the organization of collagen fibrils in different tissues (rat tendon, rat skin, liver vessels of fibrotic mice) by adjusting the pair of values $\bar{\theta}$, $std\theta$ of the theoretical distribution of supercoil angles θ (Fig. 1(d)) on the basis of the best match between experimental ρ_{exp} and theoretical ρ_{poiss} distributions, obtained by minimizing the Kolmogorov-Smirnov distance between the two empirical cumulative distribution functions associated to ρ_{exp} and ρ_{poiss} [41]. P-SHG images and maps of experimental anisotropy parameters ρ_{exp} are shown respectively in the first (a, g, m, s) and second (b, h, n, t) column of Fig. 3 for all studied tissues. Superimposed distributions of experimental ρ_{exp} (red color) and theoretical ρ_{poiss} (blue color) are shown as a function of N_{ph} in the third column (c, i, o, u) of Fig. 3. ρ_{poiss} distribution is obtained by minimizing for each interval of ten photons the Kolmogorov-Smirnov distance d_k with ρ_{exp} distribution. By doing this, ρ_{poiss} is calculated assuming the same mean number of photons N_{ph} (mean value of the interval) and thus the same Poisson parameter (see section Theory) for all pixels of each interval. A Kolmogorov-Smirnov distance D_k is then deduced from the global distributions of ρ_{exp} and ρ_{poiss} and a coefficient $R_k = 1 - D_k$ ($R_k \in [0\ 1]$), herein named correlation coefficient is deduced. Superimposed histograms of ρ_{th}(green), ρ_{poiss} (blue) and ρ_{exp} (red) are given in the fourth column (d, j, p, v) of Fig. 3. By assigning the same best matching values of $\bar{\theta}$ and $std\theta$ to the corresponding pixels of each ten photons interval, maps of $\bar{\theta}$ and $std\theta$ are shown in the fifth (e, k, q, w) and sixth (f, l, r, x) columns of Fig. 3. So, the distributions of mean number of photons N_{ph} are re-encoded into distributions of supercoil angles θ. For all simulations, the best match between ρ_{exp} and ρ_{poiss} is obtained assuming no intra pixel angular disorder ($N_f = 1$, see Discussion).

For rat EDL tendon illustrated in Figs. 3(a)–3(f), the average distribution of θ is characterized by $\bar{\theta} = 3.8$, $std\theta = 3.0$ ($R_k = 0.995$). This suggests a weak angular waving of collagen fibrils. The statistical parameters of the 9 samples studied are shown in Table 1. Moreover, histograms of Fig. 3(d) show that dispersion of ρ_{exp} is mainly due to Poisson photonic shot noise since dispersion of ρ_{th} is negligible. In addition, maps of $\bar{\theta}$ and $std\theta$ shown in Figs. 3(e) and 3(f) indicate that in plane fibrils (blue color) correspond to high N_{ph} values (Fig. 3(a), red color). Finally, from the plateau of Fig. 3(c) obtained at high photon number, the anisotropy parameter of the triple helix is deduced $\rho_0 = 1.27$ (see Eq. (1) and also the legend of Fig. 2(d)). One should notice that mean value of ρ_{exp} obtained over all pixels is $\overline{\rho_{exp}} = 1.34 \pm 0.03$ (see Table 1). This value is slightly smaller than 1.4 ± 0.03 found in rat-tails tendon taking into account birefringence and diattenuation [18] suggesting that SHG images were acquired at about 5µm depth (see Materials and Methods). Since it has been shown that in 50% glycerol cleared tissue (like our rat EDL tendon and skin samples) polarization curves remain unchanged up to 200 µm [16], we assume that birefringence and diattenuation should have a marginal effect on $\bar{\theta}$ and $std\theta$ in our experimental conditions, and therefore have not been taken into account in this study.

For rat skin illustrated in Figs. 3(g)–3(l), we found that dispersion of ρ_{exp} is characterized by a larger average supercoil angle $\bar{\theta} = 16.2$ and a stronger fibrillar waving $std\theta = 6.0$ (R_k=0.98), in agreement with the theoretical simulation of Fig. 2(c). The statistical parameters of the 9 samples studied are shown in Table 1.

For control mouse liver vessels, as illustrated in Figs. 3(m)–3(r), we found $\bar{\theta} = 16.2$ and $std\theta = 6.7$ (R_k=0.97). The statistical parameters from 32 samples studied are shown in Table 1.

For fibrotic mouse liver vessels, as illustrated in Figs. 3(s)–3(x), we found that $\bar{\theta} = 13.4$ is significantly reduced ($p = 0.006$) compared to control vessels, while $std\theta = 8.5$ is almost

Optics EXPRESS

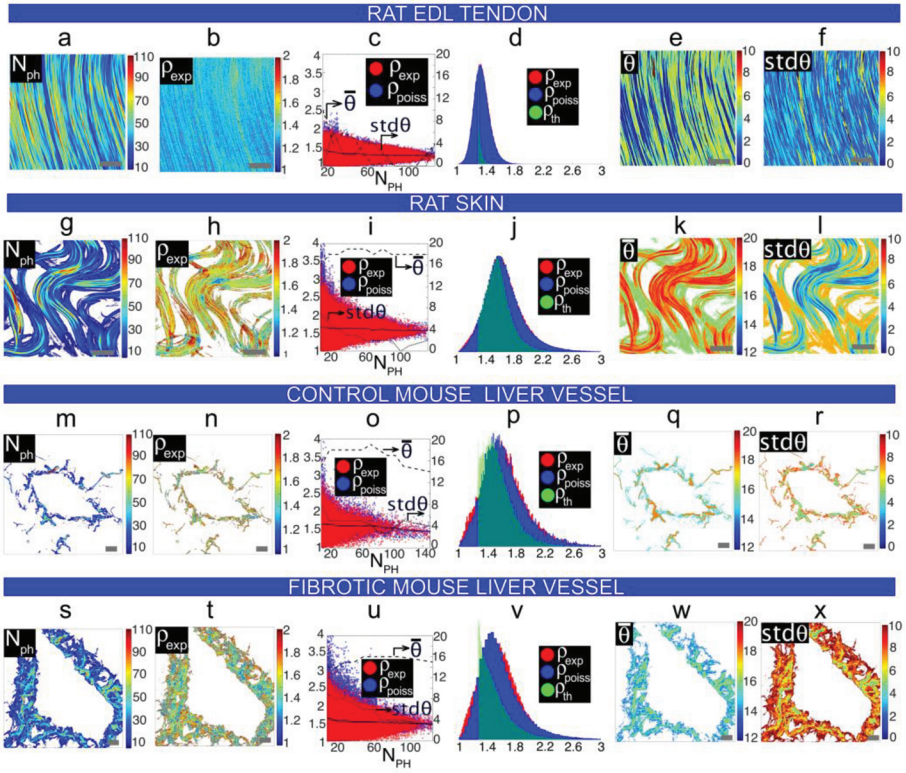

Fig. 3. P-SHG image analysis in tendon, skin and liver vessels. (first column: a, g, m, s) Typical 512×512 pixels SHG image obtained from average of the P-SHG stack. The color bar represents the mean photons number per pixel N_{ph}. Scale bar is 10 µm. (Second column: b, h, n, t) Map of the experimental anisotropy parameterρ_{exp}. (Third column: c, i, o, u) Distributions of ρ_{exp}, ρ_{poiss} as a function of N_{ph}. (Fourth column: d, j, p, v) Normalized histograms ofρ_{exp}, ρ_{poiss} and ρ_{th} distributions. (Fifth column: e, k, q, w) Map of $\bar{\theta}$ determined by affecting their values obtained in each ten photons interval to corresponding pixels (see third column). (Sixth column: f, l, r, x) Map of $std\theta$ determined by affecting their values obtained in each ten photons interval to corresponding pixels (see third column).

Table 1. Statistical parameters for tendon, skin, control (Oil-W8) and fibrotic (CCl_4-W8) liver vessels

	Rat Tendon	Rat Skin	Oil-W8	CCl_4-W8
N_{ph}	37	23	20	20
$\overline{\rho_{exp}}$	1.34 ± 0.03	1.63 ± 0.03	1.68 ± 0.07	1.62 ± 0.05**
$std\,\rho_{exp}$	0.14	0.29	0.38	0.32
$\bar{\theta}$	2.2 ± 1.8	16.2 ± 1.3	16.3 ± 2.1	14.7 ± 1.9**
$std\,\theta$	4.3	5.8	7.5	7.4
R_k	0.98	0.98	0.96	0.96
n	9	9	32	23

All values correspond to mean values for n samples. $\bar{\theta}$ and $std\theta$ correspond to mean value and dispersion of the normal distribution of supercoil angles θ that best describes the dispersion ofρ_{exp}. R_k is the correlation coefficient between ρ_{exp} and ρ_{poiss} distributions. All angles are in degrees. ** has the following t-test statistical meaning: $0.001 < p < 0.01$, between fibrotic and control liver vessels.

Optics EXPRESS

unchanged ($R_k = 0.97$). The statistical parameters from 23 samples studied are also shown in Table 1.

For tendon, skin and liver vessels, a good inverse correlation between $std\theta$ and N_{ph} is observed (Fig. 3, third column; compare also first and last columns) indicating a lower fibrillar undulation at high photon level. In other words, fibrillar undulation increases dispersion of ρ_{exp}. The results show that the fibrillar undulation $std\theta$ increases from tendon to vessels (see Fig. 3, last column and also Table 1), which is consistent with a reduction of the spatial variation of the SHG intensity along each fibril as can be seen in first column of Fig. 3. The results also suggest for the first time to our knowledge that the distribution of experimental anisotropy parameters ρ_{exp} in vessels can be explained by a variation of the supercoil angles θ. Since the mechanical properties of collagen fibrils in the toe and heel regions of the stress-strain curves is characterized by straightening of molecular kinks [42–46], the significant reduction of average angles θ in fibrotic vessels compared to control ones should corresponds to collagen fibrils elongation. This should result in an enhancement of the elastic Young's modulus and therefore contributing to the stiffness of the fibrotic vessels.

6. Discussion

The novelty of this study is that it addresses the origin of the dispersion of experimental anisotropy parameters ρ_{exp} values measured from P-SHG experiments in collagen tissues. To this aim, a simple model is used to convert dispersion of ρ into distributions of supercoil angles θ. We hypothesize that the angular dispersion of supercoil angles θ could be correlated with fibrillar undulations observed at EM level [24,28–31]. The results of our model given in Table 1 agree with those of EM studies [22,23,27]. Hence, for tendon we found $\bar{\theta} = 2.2° \pm 1.8°$ versus $\bar{\theta} \leq 5°$ for rat tendon [21]. For skin, we found $\bar{\theta} = 16.2° \pm 1.3°$ versus $\bar{\theta} = 18.4° \pm 2.8°$ for rat skin [23,26]. In addition, other EM studies in dermis have shown $\bar{\theta} \simeq 18°$ [24,27]. For liver vessels, we found $\bar{\theta} = 16.3° \pm 2.1°$ versus $\bar{\theta} = 17° \pm 3.6°$ for bovine aorta [23]. In our model, a good correlation ($R_k > 0.95$) between ρ_{exp} and ρ_{poiss} is obtained assuming no intra pixel fibrillar disorder, otherwise a drastic reduction of R_k occurs as previously shown [15]. For example, for liver vessels and for skin, R_k is reduced respectively from 0.96 to less than 0.9 and from 0.98 to 0.92. The absence of intra pixel fibrillar disorder suggests that all fibrils are aligned within each pixel, and this could be explained by interfibrillar cross-linking properties underlying the assembly of fibrils into fibers (bundle of fibrils).

It is worth to note that in the analysis of all SHG images, pixels have been thresholded above 5 photons. As a consequence the greatest value of supercoil angular dispersion calculated from the model is found in liver vessels and is about $std\,\theta = 7.5°$. It is also useful to recall that supercoil angle θ is determined from fibril main axis that is supposed to be in the plane of the microscope stage. This assumption hold in our experimental conditions for collagen tendon and skin since experimental anisotropy parameters ρ_{exp} values found (respectively ~1.3 in tendon and ~1.5 in skin) at high photon level correspond to values found for in plane fibrils [11,12,47]. Moreover, the dispersion of ρ_{exp} is fully explained by Poisson photonic shot noise (blue and red histograms of Fig. 3 fully superimpose). For liver vessels, ρ_{exp} values found at high photon level (5% of the pixels) are similar to those found in skin suggesting that corresponding fibrils are in plane. For the remaining pixels (95%), Poisson photonic shot noise alone cannot explain dispersion of ρ_{exp} assuming that fibrils are in plane (compare blue and red histograms of Figs. 3(p) and 3(v)). Indeed, dispersion of ρ_{exp} that is correlated to dispersion of θ is greater in vessels compared to skin (see Table 1) suggesting an additional contribution due to tilted fibrils that is not considered by the model. Assuming that $std\,\theta$ is similar in skin and control liver vessels, the differential value of ρ_{exp} could be explained by a tilt of less than 5° (assuming that tilt angular dependence of ρ is approximately given by Fig. 2(a)). Another way to estimate the contribution of tilted fibrils in $std\,\theta$ is to compare the values found in skin and liver vessels. The observed difference of about

Optics EXPRESS

2° (see Table 1) can be attributed to tilt. Alltogether, neglecting the tilt contribution in our model migth lead to an error below 5° in the estimation of θ.

We have addressed the sensitivity of our adjustment method between experimental ρ_{exp} and theoretical ρ_{poiss} distributions by mapping correlation coefficient r_k as a function of $\bar{\theta}$ and $std\theta$ for tendon, skin and liver vessels obtained for each interval of ten photons. Maps of r_k corresponding to the data of Fig. 3 are shown in Fig. 4. At low photon level, several couples of $\bar{\theta}$, $std\theta$ values (brown color) are close to the same maximum r_k value but at high photon level, the results show that the intra fibrillar structure of fibrils of tendon are straight while those of skin and vessels are supercoiled. Moreover, at low photon level, fibrotic liver vessels have lower supercoil $\bar{\theta}$ values (14.7°) than control vessels (16.3°) (see also Table 1), suggesting that supercoil angles might be regulated by physio pathological conditions of the tissue that need to be determined. The reduction of $\bar{\theta}$, that results in increasing the stiffness of the extracellular matrix, is probably induced by mechanical traction along fibril axis [48–51]. As a consequence, an increase rigidity of vascular wall and a subsequent rise in intra-portal tracts and central veins tone are expected [52].

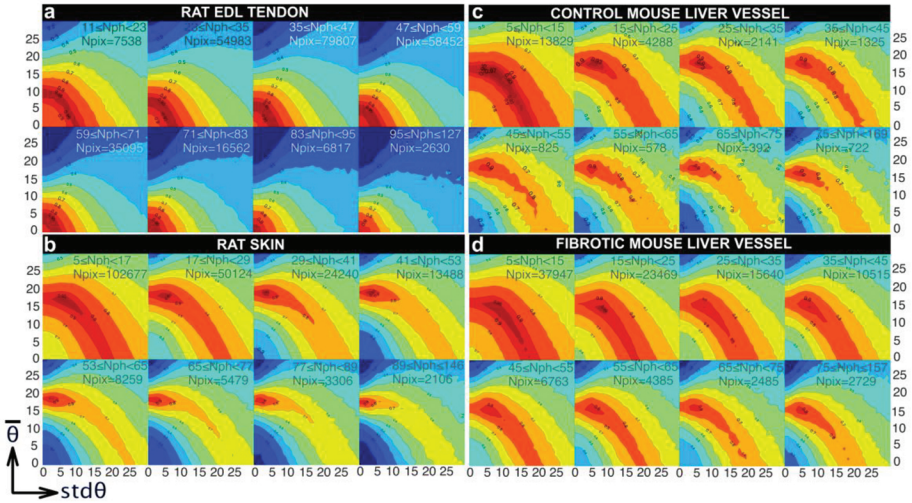

Fig. 4. Maps of correlation coefficient r_k between ρ_{exp} and ρ_{poiss} distributions as a function of θ and $std\theta$ for intervals of ten photons for (a) Rat EDL tendon (b) Rat skin (c) Control liver vessel (d) Fibrotic liver vessel. Data correspond to samples of Fig. 3. Note that to avoid a great reduction of the number of pixels for the last map, its range of photons has been increased. Note that number of photons N_{ph} and of pixels N_{pix} are indicated for the eight maps. All angles are in degrees. Note also that maps in panel (c) are characterized by rough lines. This is due to the fact that control mouse liver vessels are characterized by fewer collagen-based pixels compared to fibrotic ones (see also Fig. 3). Consequently, the standard deviations of the r_k statistics which are estimated from less data are greater, which explains the roughness of the lines.

We have noticed that for most collagen tissues studied, the average number of photons N_{ph} for a SHG image is between 20 and 50 (see Table 1). In this range of photon numbers, the Poisson photonic shot noise impacts the values of the experimental anisotropy parameter ρ_{exp} (see Figs. 2(d)–2(f)). However, thresholding above 50 photons to avoid Poisson photonic shot noise will result in a great loss of information concerning the wavy nature of fibrils. Alternatively, increasing the acquisition time will improve the signal to noise ratio, but the disadvantage is probably the presence of more artifacts related to mechanical drift. For example, with our

Optics EXPRESS

experimental setup, the acquisition of a 512×512 pixels SHG image with a duration of one second gives ~ 20 photons per pixel due to the 5 MHZ bandwidth limit of the high sensitivity single photon GasAsP photomultiplier (H7421-40) provided by Hamamatsu. In a usual P-SHG acquisition, a compromise between acquisition duration and signal to noise ratio is mandatory. We found that a maximum photons number around 100 is a good compromise. Overall, our study indicates that an accurate estimate of fibrillar disorder from a P-SHG experiment is possible regardless of the number of photons per pixel as long as Poisson photonic shot noise is considered.

Our model enables an efficient conversion of the dispersion of ρ values into a dispersion of supercoil angles θ. However, it does not take into account either chiral components of the nonlinear susceptibility tensor that appear for tilted fibrils [53] or axial components of the electric fields induced by high numerical aperture (NA) [54,55] while both factors could impact an accurate determination of ρ. Concerning chirality, we assume its contribution to be negligible in the determination of ρ because we estimated that collagen fibrils of tendon and skin are in plane and those of liver vessels have tilt angles less than 5°. Since the simulation is based on the plane wave approximation, it does not consider axial components of the electric fields induced by high numerical aperture (NA) objective like those used in our experiment (60XW, NA = 1.2, see section Materials and methods). For vessels, we found a reduction of ρ_{exp} values of about 0.15 when using low NA objective (20X, NA = 0.75). This is in agreement with the theoretical prediction of about 0.05 obtained for the same NA variation [54,55]. Therefore, ρ_{exp} and ρ_0 are overestimated by using high NA objective, and in consequence supercoil angles are also overestimated. According to Fig. 2(a), fluctuation of ρ of 0.15 corresponds to an angle variation of about 5° that still remains a good estimate of θ for all collagen tissues, and in good agreement with values found in EM studies.

7. Conclusion

In this study, we have calculated the second-order nonlinear optical anisotropy parameter $\rho = \chi_{ZZZ}/\chi_{ZXX}$ for collagen-rich tissues assuming the same model of wavy collagen fibril with a variable supercoil angle θ. The results highlight that the wavy nature of collagen fibrils can be deduced from distributions of experimental ρ values taking into account the Poisson photonic shot noise of the detection system. Furthermore, the results suggest that the stiffness of fibrotic liver is due to a remodeling of the extracellular matrix which reduces the average value of θ. These results open new avenue for future modeling that correlates the dispersion of ρ values in P-SHG experiments and the fibrillar architecture as well as the mechanical stiffness of patho-physiological extracellular matrices in collagen tissues.

Appendix: Derivation of the SHG anisotropy parameter $\rho_{th} = \chi_{ZZZ}/\chi_{ZXX}$.

According to the helical symmetry of the collagen triple helix molecule, its nonlinear optical hyperpolarizability $\beta^{(2)}$ is described by only two independent tensor elements $\beta_{Z_0Z_0Z_0}$ and $\beta_{Z_0X_0X_0} = \beta_{Z_0Y_0Y_0} = \beta_{X_0X_0Z_0} = \beta_{Y_0Y_0Z_0} = \beta_{X_0Z_0X_0} = \beta_{Y_0Z_0Y_0}$ [9,12,32], when written in coordinate system (X_0, Y_0, Z_0) where Z_0 is the main axis of the triple helix (Fig. 1(a)). Considering that the triple helix can be wrapped with an angle θ around the collagen main fibril axis Z in coordinate system (X, Y, Z) associated to the fibril (Fig. 1(a)), components of $\beta^{(2)}$ expressed in this reference frame are given by the following tensor transformation [56]

$$\beta_{IJK} = \sum_{I_0J_0K_0} R_{II_0}R_{JJ_0}R_{KK_0}\,\beta_{I_0J_0K_0}. \tag{3}$$

Optics EXPRESS

R_{II_0} is any component of the Euler matrix $R(\Omega)$ that transforms between (X_0, Y_0, Z_0) and (X, Y, Z) coordinate systems [57]

$$R(\Omega) = \begin{pmatrix} \cos\varphi\cos\theta & -\sin\varphi & \cos\varphi\sin\theta \\ \sin\varphi\cos\theta & \cos\varphi & \sin\varphi\sin\theta \\ -\sin\theta & 0 & \cos\theta \end{pmatrix}. \tag{4}$$

Euler angles θ, φ refer to polar and azimuthal angles (Fig. 1(a)). As a rule, macroscopic second-order nonlinear optical susceptibility $\chi^{(2)}$ at pixel level is obtained from $\beta^{(2)}$ by summing the contribution of all the nonlinear molecular sources within the focusing volume [58–60]. In the case where the incident IR beam light propagates in the Y direction (Fig. 1(f)), the only components of $\chi^{(2)}$ that participate to the SHG intensity are χ_{ZZZ}, χ_{ZXX}, $\chi_{XXZ} = \chi_{XZX}$, and χ_{XXX}, χ_{XZZ}, $\chi_{ZXZ} = \chi_{ZZX}$ when expressed in coordinate system X, Y, Z, and if restricted to the plane wave approximation $E_Y^\omega = 0$ [61]. In consequence, only the corresponding components of $\beta^{(2)}$ need to be calculated. Assuming that collagen main fibril axis Z lies in the plane of the microscope stage (Fig. 1(f)), we found that only four coefficients β_{ZZZ}, $\beta_{ZXX} = \beta_{XXZ} = \beta_{XZX}$, β_{XXX}, $\beta_{XZZ} = \beta_{ZXZ} = \beta_{ZZX}$ are independent, and they are given by

$$\begin{pmatrix} \beta_{ZZZ} \\ \beta_{ZXX} \\ \beta_{XXX} \\ \beta_{XZZ} \end{pmatrix} = \begin{pmatrix} \cos^3\theta & 3\cos\theta\sin^2\theta \\ \cos\theta\sin^2\theta\cos^2\varphi & \cos\theta - 3\cos\theta\sin^2\theta\cos^2\varphi \\ \sin^3\theta\cos^3\varphi & 3\sin\theta\cos\varphi - 3\sin^3\theta\cos^3\varphi \\ \sin\theta\cos^2\theta\cos\varphi & \sin\theta(1-3\cos^2\theta)\cos\varphi \end{pmatrix} \begin{pmatrix} \beta_{Z_0Z_0Z_0} \\ \beta_{Z_0X_0X_0} \end{pmatrix}. \tag{5}$$

Considering that each pixel may contain N_f fibrils f (supposed identical for simplicity) but with different polar angles θ^f (see Fig. 1(e)) measured from the same direction Z, the corresponding second-order nonlinear optical susceptibility coefficients are deduced

$$\begin{pmatrix} \chi_{ZZZ} \\ \chi_{ZXX} \\ \chi_{XXX} \\ \chi_{XZZ} \end{pmatrix} = N \begin{pmatrix} \left\langle \cos^3\theta^f \right\rangle & 3\left\langle \cos\theta^f \sin^2\theta^f \right\rangle \\ \left\langle \cos\theta^f \sin^2\theta^f \left\langle \cos^2\varphi \right\rangle_f \right\rangle & \left\langle \cos\theta^f \right\rangle - 3\left\langle \cos\theta^f \sin^2\theta^f \left\langle \cos^2\varphi \right\rangle_f \right\rangle \\ \left\langle \sin^3\theta^f \left\langle \cos^3\varphi \right\rangle_f \right\rangle & 3\left\langle \sin\theta^f \left\langle \cos\varphi \right\rangle_f \right\rangle - 3\left\langle \sin^3\theta^f \left\langle \cos^3\varphi \right\rangle_f \right\rangle \\ \left\langle \sin\theta^f \cos^2\theta^f \left\langle \cos\varphi \right\rangle_f \right\rangle & \left\langle \sin\theta^f (1-3\cos^2\theta^f) \langle \cos\varphi \rangle_f \right\rangle \end{pmatrix} \begin{pmatrix} \beta_{Z_0Z_0Z_0} \\ \beta_{Z_0X_0X_0} \end{pmatrix}, \tag{6}$$

where N is the triple helix concentration and $\left\langle h(\theta^f) \right\rangle \triangleq N_f^{-1} \sum_{f=1}^{N_f} h(\theta^f)$ corresponds to a discrete summation over N_f. $\langle g(\varphi) \rangle_f \triangleq \frac{1}{\Delta\varphi} \int_{\varphi_0^f}^{\varphi_0^f + \Delta\varphi} g(\varphi) d\varphi$ denotes mean value on the part of each fibril f of pitch P that is contained in the transverse PSF. Indeed, for skin and vessels, the pitch P is about 1 µm [22,62], which is greater than the size of the transverse PSF ($w_T = 0.4\mu m$, see section Materials and methods) such that $\Delta\varphi = 2\pi \times w_T / P$. For tendon, P~20 µm is estimated from the SHG images by the average distance between two maximums along each fibril (see Fig. 3(a)). Otherwise, φ_0^f is randomly chosen for each fibril f. χ_{XXX} and χ_{XZZ} are considered here weak because mean values $\langle g(\varphi) \rangle_f$ are distributed around zero. In the particular case of an average of φ over a full turn of the coiling, these coefficients are exactly zeros. Moreover, we have verified numerically that they contribute generally to less than 10% to the SHG signal in our experimental conditions ($\theta^f \leq 25°$ for all experimental results), and for this reason they have been neglected in the expression of the SHG intensity. Theoretical SHG anisotropy parameter $\rho_{th} = \chi_{ZZZ} / \chi_{ZXX}$ of

Optics EXPRESS

each pixel is deduced from Eq. (6)

$$\rho_{th} = \frac{\rho_0 \left\langle \cos\theta^f \right\rangle + (3-\rho_0)\left\langle \cos\theta^f \sin^2\theta^f \right\rangle}{\left\langle \cos\theta^f \right\rangle - (3-\rho_0)\left\langle \left\langle \cos^2\varphi \right\rangle_f \cos\theta^f \sin^2\theta^f \right\rangle}, \tag{7}$$

where $\rho_0 = \beta_{Z_0Z_0Z_0}/\beta_{Z_0X_0X_0}$ is defined as the anisotropy parameter of the triple helix. Equation (7) corresponds to Eq. (1) of the main text. When all the fibrils within the pixel have the same polar angle $\theta^f = \theta$ (no intra pixel disorder), then $N_f = 1$ and $\left\langle h(\theta^f) \right\rangle = h(\theta)$ in the above equation. If in addition, the average of φ is carried out on a full turn of the supercoil helix then $<\cos^2\varphi> = \frac{1}{2}$, and the resulting expression of ρ_{th} is identical to Eq. (1) of Ref. [12].

Funding

Région Bretagne; Rennes Métropole; Conseil Général d'Ille-et-Vilaine; Valorial Rennes; Ministère de l'Education Nationale, de l'Enseignement Supérieur et de la Recherche; European Union Federal Funds.

Disclosures

The authors declared no conflicts of interest.

References

1. I. Freund, M. Deutsch, and A. Sprecher, "Connective-tissue polarity - optical 2nd-harmonic microscopy, crossed-beam summation, and small-angle scattering in rat-tail tendon," Biophys. J. **50**(4), 693–712 (1986).
2. P. J. Campagnola and L. M. Loew, "Second-harmonic imaging microscopy for visualizing biomolecular arrays in cells, tissues and organisms," Nat. Biotechnol. **21**(11), 1356–1360 (2003).
3. P. J. Campagnola, A. C. Millard, M. Terasaki, P. E. Hoppe, C. J. Malone, and W. A. Mohler, "Three-dimensional high-resolution second-harmonic generation imaging of endogenous structural proteins in biological tissues," Biophys. J. **82**(1), 493–508 (2002).
4. W. R. Zipfel, R. M. Williams, and W. W. Webb, "Nonlinear magic: multiphoton microscopy in the biosciences," Nat. Biotechnol. **21**(11), 1369–1377 (2003).
5. S. V. Plotnikov, A. C. Millard, P. J. Campagnola, and W. A. Mohler, "Characterization of the myosin-based source for second-harmonic generation from muscle sarcomeres," Biophys. J. **90**(2), 693–703 (2006).
6. F. Tiaho, G. Recher, and D. Rouede, "Estimation of helical angles of myosin and collagen by second harmonic generation imaging microscopy," Opt. Express **15**(19), 12286–12295 (2007).
7. S. Psilodimitrakopoulos, D. Artigas, G. Soria, I. Amat-Roldan, A. M. Planas, and P. Loza-Alvarez, "Quantitative discrimination between endogenous SHG sources in mammalian tissue, based on their polarization response," Opt. Express **17**(12), 10168–10176 (2009).
8. S. Brasselet, "Polarization-resolved nonlinear microscopy: application to structural molecular and biological imaging," Adv. Opt. Photonics **3**(3), 205–271 (2011).
9. A. Tuer, S. Krouglov, R. Cisek, D. Tokarz, and V. Barzda, "Three-dimensional visualization of the first hyperpolarizability tensor," J. Comput. Chem. **32**(6), 1128–1134 (2011).
10. X. Chen, O. Nadiarynkh, S. Plotnikov, and P. J. Campagnola, "Second harmonic generation microscopy for quantitative analysis of collagen fibrillar structure," Nat. Protoc. **7**(4), 654–669 (2012).
11. I. Gusachenko, V. Tran, Y. G. Houssen, J. M. Allain, and M. C. Schanne-Klein, "Polarization-Resolved Second-Harmonic Generation in Tendon upon Mechanical Stretching," Biophys. J. **102**(9), 2220–2229 (2012).
12. A. E. Tuer, M. K. Akens, S. Krouglov, D. Sandkuijl, B. C. Wilson, C. M. Whyne, and V. Barzda, "Hierarchical model of fibrillar collagen organization for interpreting the second-order susceptibility tensors in biological tissue," Biophys. J. **103**(10), 2093–2105 (2012).
13. P.-J. Su, W.-L. Chen, Y.-F. Chen, and C.-Y. Dong, "Determination of collagen nanostructure from second-order susceptibility tensor analysis," Biophys. J. **100**(8), 2053–2062 (2011).
14. D. Rouede, J. J. Bellanger, J. Bomo, G. Baffet, and F. Tiaho, "Linear least square (LLS) method for pixel-resolution analysis of polarization dependent SHG images of collagen fibrils," Opt. Express **23**(10), 13309–13319 (2015).
15. D. Rouede, E. Schaub, J. J. Bellanger, F. Ezan, J. C. Scimeca, G. Baffet, and F. Tiaho, "Determination of extracellular matrix collagen fibril architectures and pathological remodeling by polarization dependent second harmonic microscopy," Sci. Rep. **7**(1), 12197 (2017).
16. O. Nadiarnykh and P. J. Campagnola, "Retention of polarization signatures in SHG microscopy of scattering tissues through optical clearing," Opt. Express **17**(7), 5794–5806 (2009).

Optics EXPRESS

17. S. Brasselet, D. Aït-Belkacem, A. Gasecka, F. Munhoz, S. Brustlein, and S. Brasselet, "Influence of birefringence on polarization resolved nonlinear microscopy and collagen SHG structural imaging," Opt. Express **18**(14), 14859–14870 (2010).
18. I. Gusachenko, G. Latour, and M.-C. Schanne-Klein, "Polarization-resolved second harmonic microscopy in anisotropic thick tissues," Opt. Express **18**(18), 19339–19352 (2010).
19. A. Rich and F. H. C. Crick, "The molecular structure of collagen," J. Mol. Biol. **3**(5), 483–IN4 (1961).
20. J. W. Smith, "Molecular pattern in native collagen," Nature **219**(5150), 157–158 (1968).
21. V. Ottani, M. Raspanti, and A. Ruggeri, "Collagen structure and functional implications," Micron **32**(3), 251–260 (2001).
22. M. Bouteille and D. C. Pease, "The tridimensional structure of native collagenous fibrils, their proteinaceous filaments," J. Ultrastruct. Res. **35**(3-4), 314–338 (1971).
23. M. Raspanti, V. Ottani, and A. Ruggeri, "Different architectures of the collagen fibril: morphological aspects and functional implications," Int. J. Biol. Macromol. **11**(6), 367–371 (1989).
24. A. Ruggeri, F. Benazzo, and E. Reale, "Collagen fibrils with straight and helicoidal microfibrils: a freeze-fracture and thin-section study," J. Ultrastruct. Res. **68**(1), 101–108 (1979).
25. D. G. Rayns, "Collagen from frozen fractured glycerinated beef heart," J. Ultrastruct. Res. **48**(1), 59–66 (1974).
26. J. C. Belton, D. Michaeli, and H. H. Fudenberg, "Freeze-etch study of collagen. I. Native collagen from tendon and lung of rats," Arthritis Rheum. **18**(5), 443–450 (1975).
27. J. H. Lillie, D. K. MacCallum, L. J. Scaletta, and J. C. Occhino, "Collagen structure: evidence for a helical organization of the collagen fibril," J. Ultrastruct. Res. **58**(2), 134–143 (1977).
28. O. Ohtani, "Three-dimensional organization of the collagen fibrillar framework of the human and rat livers," Arch. Histol. Cytol. **51**(5), 473–488 (1988).
29. J. Diamant, A. Keller, E. Baer, M. Litt, and R. G. Arridge, "Collagen; ultrastructure and its relation to mechanical properties as a function of ageing," Proc. R. Soc. Lond. B **180**(1060), 293–315 (1972).
30. J. H. Evans and J. C. Barbenel, "Structural and mechanical properties of tendon related to function," J. Equine Vet. Sci. **7**(1), 1–8 (1975).
31. M. Franchi, V. Ottani, R. Stagni, and A. Ruggeri, "Tendon and ligament fibrillar crimps give rise to left-handed helices of collagen fibrils in both planar and helical crimps," J. Anat. **216**(3), 301–309 (2010).
32. A. Deniset-Besseau, J. Duboisset, E. Benichou, F. Hache, P. F. Brevet, and M. C. Schanne-Klein, "Measurement of the second-order hyperpolarizability of the collagen triple helix and determination of its physical origin," J. Phys. Chem. B **113**(40), 13437–13445 (2009).
33. I. Freund and M. Deutsch, "Macroscopic polarity of connective tissue is due to discrete polar structures," Biopolymers **25**(4), 601–606 (1986).
34. K. Tilbury, C. H. Lien, S. J. Chen, and P. J. Campagnola, "Differentiation of col I and col III isoforms in stromal models of ovarian cancer by analysis of second harmonic generation polarization and emission directionality," Biophys. J. **106**(2), 354–365 (2014).
35. S. Roth and I. Freund, "Optical second-harmonic scattering in rat-tail tendon," Biopolymers **20**(6), 1271–1290 (1981).
36. S. W. Chu, S. Y. Chen, G. W. Chern, T. H. Tsai, Y. C. Chen, B. L. Lin, and C. K. Sun, "Studies of chi(2)/chi(3) tensors in submicron-scaled bio-tissues by polarization harmonics optical microscopy," Biophys. J. **86**(6), 3914–3922 (2004).
37. R. M. Williams, W. R. Zipfel, and W. W. Webb, "Interpreting second-harmonic generation images of collagen I fibrils," Biophys. J. **88**(2), 1377–1386 (2005).
38. D. Aït-Belkacem, M. Guilbert, M. Roche, J. Duboisset, P. Ferrand, G. Sockalingum, P. Jeannesson, and S. Brasselet, "Microscopic structural study of collagen aging in isolated fibrils using polarized second harmonic generation," J. Biomed. Opt. **17**(8), 080506 (2012).
39. P. Stoller, K. M. Reiser, P. M. Celliers, and A. M. Rubenchik, "Polarization-Modulated Second Harmonic Generation in Collagen," Biophys. J. **82**(6), 3330–3342 (2002).
40. J. Duboisset, D. Aït-Belkacem, M. Roche, H. Rigneault, and S. Brasselet, "Generic model of the molecular orientational distribution probed by polarization-resolved second-harmonic generation," Phys. Rev. A **85**(4), 043829 (2012).
41. W. H. Press, S. A. Teukolsky, W. T. Vetterling, and B. P. Flannery, *Numerical Recipes in FORTRAN; The Art of Scientific Computing* (Cambridge University, 1993).
42. E. Mosler, W. Folkhard, E. Knorzer, H. Nemetschek-Gansler, T. Nemetschek, and M. H. Koch, "Stress-induced molecular rearrangement in tendon collagen," J. Mol. Biol. **182**(4), 589–596 (1985).
43. N. Sasaki and S. Odajima, "Elongation mechanism of collagen fibrils and force-strain relations of tendon at each level of structural hierarchy," J. Biomech. **29**(9), 1131–1136 (1996).
44. K. Misof, G. Rapp, and P. Fratzl, "A new molecular model for collagen elasticity based on synchrotron X-ray scattering evidence," Biophys. J. **72**(3), 1376–1381 (1997).
45. P. Fratzl, K. Misof, I. Zizak, G. Rapp, H. Amenitsch, and S. Bernstorff, "Fibrillar structure and mechanical properties of collagen," J. Struct. Biol. **122**(1-2), 119–122 (1998).
46. A. Gautieri, S. Vesentini, A. Redaelli, and M. J. Buehler, "Hierarchical Structure and Nanomechanics of Collagen Microfibrils from the Atomistic Scale Up," Nano Lett. **11**(2), 757–766 (2011).

Optics EXPRESS

47. E. I. Romijn, A. Finnoy, and M. B. Lilledahl, "Analyzing the feasibility of discriminating between collagen types I and II using polarization-resolved second harmonic generation," J. Biophotonics **12**(1), e201800090 (2019).
48. I. Amat-Roldan, S. Psilodimitrakopoulos, P. Loza-Alvarez, and D. Artigas, "Fast image analysis in polarization SHG microscopy," Opt. Express **18**(16), 17209–17219 (2010).
49. A. S. Abhilash, B. M. Baker, B. Trappmann, C. S. Chen, and V. B. Shenoy, "Remodeling of fibrous extracellular matrices by contractile cells: predictions from discrete fiber network simulations," Biophys. J. **107**(8), 1829–1840 (2014).
50. M. S. Hall, F. Alisafaei, E. Ban, X. Feng, C. Y. Hui, V. B. Shenoy, and M. Wu, "Fibrous nonlinear elasticity enables positive mechanical feedback between cells and ECMs," Proc. Natl. Acad. Sci. U. S. A. **113**(49), 14043–14048 (2016).
51. S. van Helvert and P. Friedl, "Strain Stiffening of Fibrillar Collagen during Individual and Collective Cell Migration Identified by AFM Nanoindentation," ACS Appl. Mater. Interfaces **8**(34), 21946–21955 (2016).
52. M. Pinzani, S. Milani, R. De Franco, C. Grappone, A. Caligiuri, A. Gentilini, C. Tosti-Guerra, M. Maggi, P. Failli, C. Ruocco, and P. Gentilini, "Endothelin 1 is overexpressed in human cirrhotic liver and exerts multiple effects on activated hepatic stellate cells," Gastroenterology **110**(2), 534–548 (1996).
53. A. Golaraei, K. Mirsanaye, Y. Ro, S. Krouglov, M. K. Akens, B. C. Wilson, and V. Barzda, "Collagen chirality and three-dimensional orientation studied with polarimetric second-harmonic generation microscopy," J. Biophotonics **12**(1), e201800241 (2019).
54. C. Teulon, I. Gusachenko, G. Latour, and M.-C. Schanne-Klein, "Theoretical, numerical and experimental study of geometrical parameters that affect anisotropy measurements in polarization-resolved SHG microscopy," Opt. Express **23**(7), 9313–9328 (2015).
55. I. Gusachenko and M.-C. Schanne-Klein, "Numerical simulation of polarization-resolved second-harmonic microscopy in birefringent media," Phys. Rev. A **88**(5), 053811 (2013).
56. J. F. Nye, *Physical Properties of Crystals* (Oxford University Press, 1985).
57. G. B. Arfken, *Mathematical Methods for Physicists*, 6th ed. (Elsevier Academic Press, 2005).
58. J. L. Oudar and J. Zyss, "Structural dependence of nonlinear-optical properties of methyl-(2,4-dinitrophenyl)-aminopropanoate crystals," Phys. Rev. A **26**(4), 2016–2027 (1982).
59. F. Ghebremichael, M. G. Kuzyk, K. D. Singer, and J. H. Andrews, "Relationship between the second-order microscopic and macroscopic nonlinear optical susceptibilities of poled dye-doped polymers," J. Opt. Soc. Am. B **15**(8), 2294–2297 (1998).
60. B. Dick, "Irreducible tensor analysis of sum- and difference-frequency generation in partially oriented samples," Chem. Phys. **96**(2), 199–215 (1985).
61. R. Boyd, *Nonlinear Optics*, 3rd ed. (Academic Press, 2008).
62. K. Beck and B. Brodsky, "Supercoiled protein motifs: the collagen triple-helix and the alpha-helical coiled coil," J. Struct. Biol. **122**(1-2), 17–29 (1998).